Draft version July 26, 2024
Typeset using LaTeX **twocolumn** style in AASTeX631

Evolution of reconnection flux during eruption of magnetic flux ropes

Samriddhi Sankar Maity [1,2], Piyali Chatterjee [3], Ranadeep Sarkar [4] and Ijas S. Mytheen [5]

[1] *Indian Institute of Astrophysics, Bangalore-560034, India*
[2] *Joint Astronomy Programme and Department of Physics, Indian Institute of Science, Bangalore, India*
[3] *Indian Institute of Astrophysics, Bangalore, India*
[4] *University of Helsinki, Finland*
[5] *Amrita School of Physical Science, Amrita Vishwa Vidyapeetham, Kollam, India*

ABSTRACT

Coronal mass ejections (CMEs) are powerful drivers of space weather, with magnetic flux ropes (MFRs) widely regarded as their primary precursors. However, the variation in reconnection flux during the evolution of MFR during CME eruptions remains poorly understood. In this paper, we develop a realistic 3D magneto-hydrodynamic model using which we explore the temporal evolution of reconnection flux during the MFR evolution using both numerical simulations and observational data. Our initial coronal configuration features an isothermal atmosphere and a potential arcade magnetic field beneath which an MFR emerges at the lower boundary. As the MFR rises, we observe significant stretching and compression of the overlying magnetic field beneath it. Magnetic reconnection begins with the gradual formation of a current sheet, eventually culminating with the impulsive expulsion of the flux rope. We analyze the temporal evolution of reconnection fluxes during two successive MFR eruptions while continuously emerging the twisted flux rope through the lower boundary. We also conduct a similar analysis using observational data from the Helioseismic and Magnetic Imager (HMI) and the Atmospheric Imaging Assembly (AIA) for an eruptive event. Comparing our MHD simulation with observational data, we find that reconnection flux play a crucial role in determination of CME speeds. From the onset to the eruption, the reconnection flux shows a strong linear correlation with the velocity. This nearly realistic simulation of a solar eruption provides important insights into the complex dynamics of CME initiation and progression.

1. INTRODUCTION

Coronal Mass Ejections are composed of clouds of magnetized plasma that are expelled from the Sun into the heliosphere due to sudden release of free magnetic energy stored in the twisted coronal magnetic field (Chen 2017). They are of interest due to scientific and technological reasons since CMEs can drive interplanetary shocks that energize solar particles and cause significant space weather effects in the geospace. In-situ data obtained by satellites passing through the interplanetary CMEs (ICMEs) have established that typical ICMEs have the structure of highly twisted MFR (Wang et al. 2016; Hu 2017). Many CME models therefore incorporate a magnetic flux rope– consisting of helical field lines twisting about a central axis in the corona as the basic underlying magnetic field structure for CME precursors (Titov & Démoulin 1999; Gibson & Fan 2006; Duan et al. 2019; Liu 2020; Chen 2017). Therefore, understanding their evolution in early phase is crucial for CME studies.

Although is it widely accepted that MFRs constitute the core structure of the CMEs, it remains unknown wheather MFRs exist in the solar corona before CME initiation or forms during the eruption (Chen 2011; Patsourakos et al. 2020). Some opine that the MFR could exist prior to eruptions (Cheng et al. 2011), although there is no consensus on how and where an MFR might form. An alternate hypothesis is that the MFRs can bodily emerge from the below the photosphere (Fan 2001; Martínez-Sykora et al. 2008; Magara 2004; Archontis et al. 2009). Yet another proposition is that the MFRs can be built directly in the corona via shearing of magnetic footpoints and reconnection prior to the eruption (van Ballegooijen & Martens 1989; Amari et al. 2003; Aulanier et al. 2010; Chatterjee et al. 2016). Most eruptions, particularly those originating from solar active regions (ARs), occur along magnetic polarity inversion lines (PILs) within strong field regions. Furthermore, some flare-productive ARs exhibit relatively short time interval between successive eruptions, while displaying very similar structure in the flare emissions and

CME morphology. Such kind of event has been known as homologous eruptions (Zhang & Wang 2002). Observations indicate that the evolution of the source regions of homologous events is often characterized by continuous shearing motion (Li et al. 2010; Romano et al. 2015, 2018; Sarkar et al. 2019), sunspot rotation (Régnier & Canfield 2006; Zhang et al. 2008), and flux emergence (Nitta & Hudson 2001; Sterling & Moore 2001; Ranns et al. 2000; Dun et al. 2007; Xu et al. 2017).

Although numerous theories have been proposed to explain solar eruption (Forbes et al. 2006; Shibata & Magara 2011; Chen 2011; Schmieder et al. 2013; Aulanier 2014; Janvier et al. 2015) only two scenarios have been established through magnetohydrodynamics (MHD) simulations for explaining homologous eruptions, namely the breakout model (DeVore & Antiochos 2008) and flux emergence model (Chatterjee & Fan 2013). The breakout mechanism relies on a multipolar magnetic topology with a magnetic null point situated above a core flux that is shared by photospheric motion. An eruption is triggered by magnetic reconnection at the null point which removes the overlying restraining field of the shared core and after the eruption the null point topology restored (Antiochos et al. 1999; Wyper et al. 2017; Lynch et al. 2008). DeVore & Antiochos (2008) showed that, by imposing a continual shearing motion can produce homologous eruptions, which are however confined without producing CMEs. Magnetic flux emergence, in which new flux rises from the convection zone, where the turbulent convection can create twisted magnetic field lines, is another mechanism believed to initiate eruptions (Chen & Shibata 2000; Archontis & Hood 2008; Fan 2010). Chatterjee & Fan (2013) demonstrated occurrence of homologous CMEs driven by the emergence of a highly twisted flux tube into the solar corona. In their simulation, the coronal flux rope partially erupted and reformed, repeatedly. However, the time interval between two successive eruptions was too short for the post-eruption field of the first one to relax and restore an equilibrium before the second eruption.

Although magnetic reconnection can only be indirectly observed, it is a critical process in the solar corona that forms closed loops and energizes the plasma and particles leading to impulsively enhanced flare radiation. The observed correlation between the evolution of the CME kinematics and that of the flare X-ray fluxes suggests that the CME eruption is related to the reconnection (Zhang et al. 2001; Temmer et al. 2008; Bein et al. 2012; Patsourakos et al. 2013), consistent with CME initiation models (Chen 2011). Magnetic reconnection almost always occurs during a CME eruption yet it remains unclear whether reconnection initiates the eruption or a consequence. The morphological evolution of flare emission in the lower atmosphere has also been used to infer the reconnection process in the corona (Forbes & Priest 1984; Kopp & Poletto 1986). Due to the difficulty in observing CME evolution and measuring CME acceleration in the low corona, many studies instead compare the CME velocity measured at a few solar radii after the peak acceleration phase and the total magnetic flux reconnected during the flare. Note that most of the studies have focused on at a instant after the peak phase and it is unclear weather the evolution flux is at all related to the velocity. Numerical MHD simulations have proven to be powerful tools for reproducing the time-dependent, nonlinear evolution of 3D magnetic configurations and investigating the temporal changes in flux during the early phases of magnetic flux rope (MFR) eruptions. A key property characterizing solar flares is the amount of magnetic flux passing through the reconnection sheet beneath the MFR, commonly referred to as the reconnection flux (Gopalswamy et al. 2017). While the reconnected flux cannot be measured directly from observations of the corona, a quantitative relationship between the reconnection flux in the corona is the magnetic flux swept by the flare ribbon or the foot points of the MFR (Kazachenko et al. 2017; Qiu et al. 2004).

In this paper, we conduct a 3-dimensional compressible MHD simulation to study the time evolution of the reconnection flux and correlate it with the velocity of the MFR during its early evolution. We further compare our analysis with an observed event. The observational data

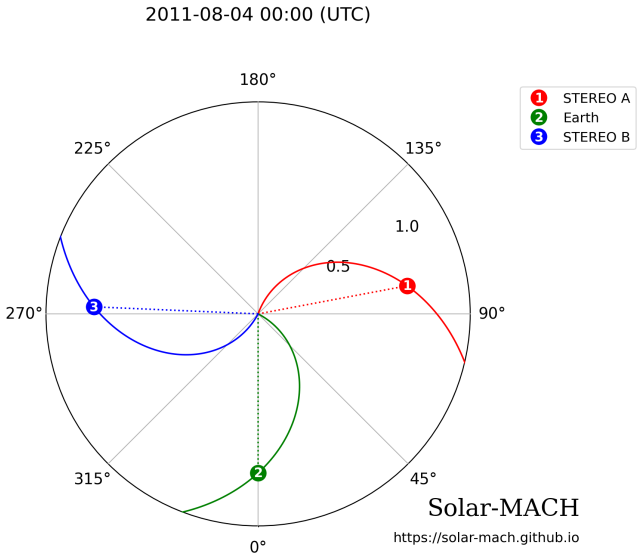

Figure 1. Location of STEREO spacecraft and Earth on 2011 August 4.

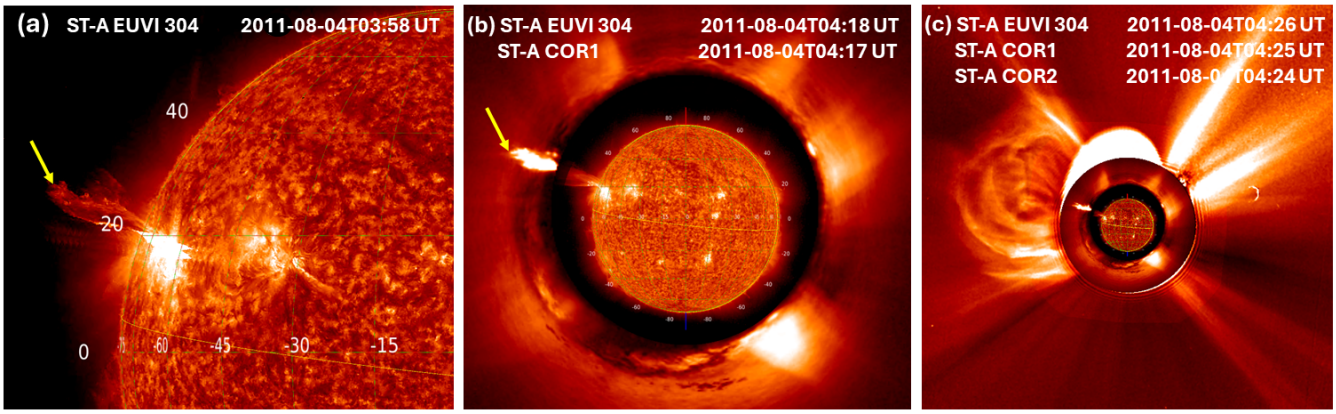

Figure 2. Different phases of the filament eruption on 2011 August 04 as observed by STEREO-A. (a) Image of the Sun in STEREO-A EUVI 304 Å (b) COR1 image superimposed with STEREO-A EUVI 304 Å (c) Superimposed images of STEREO-A EUVI 304 Å , COR1 and COR2. The yellow arrows in panels (a) and (b) indicate the filament leading edge. The images are plotted using JHelioviewer (https://www.jhelioviewer.org/).

and methods is mentioned in Section 2, the numerical setup is presented in Section 3. The results are mentioned in Section 4 and we conclude with a summary in Section 5.

2. OBSERVATION DATA

We study the temporal evolution of re-connection flux and the associated CME speed during the M-class flare (SOL2011-SOL2011-08-04T03:41) which occurred in AR 11261 during 2011 August 4. During this period, STEREO-A and STEREO-B were positioned at longitudinal separations of 101° and 92° (see Figure 1), respectively, relative to the Sun-Earth line. This positioning allowed the two spacecraft to provide near-limb views of Earth-directed CMEs. On the other hand the location of AR 11261 was close to the solar disk center (between 30°to 35° west) relative to Earth, offering reliable data on the solar magnetic field of the AR. This provides a unique opportunity to study the co-temporal evolution of re-connection flux, estimated from on-disk SDO data, and the speed of the associated eruption, starting from the initiation height at lower corona as observed from near-limb observations by STEREO.

We analyze the kinematics of the eruption associated with the M-class flare on 2011 August 04, by tracking the filament leading-edge height as observed by STEREO-A. We use two instruments from the Sun Earth Connection Coronal and Heliospheric Investigation (SECCHI; Howard et al. (2008)) onboard STEREO-A to track the early evolution of the Earth-directed filament eruption, which was observed as prominence eruption from STEREO-A (see Figure 2). The instruments include the Extreme Ultraviolet Imager (EUVI; $< 1.7R_{\odot}$, Wuelser et al. (2004)) and the inner coronagraph COR1 ($1.3 - 4R_{\odot}$, Thompson et al. (2003)).

We follow the method by (Kazachenko 2023), to estimate the temporal profile of reconnecting flux. The observations of the flare ribbons are obtained from the Atmospheric Imaging Assembly (AIA; Lemen et al. (2012)) onboard SDO in 1600 Å channel. The associated full-disk magnetograms are obtained from the Helioseismic and Magnetic Imager (HMI; Schou et al. (2012)). During the recurrent eruptive M-class flare in AR 11261 on 2011 August 4, we identify the area swept out by the flare-ribbons observed in AIA 1600 Å images as shown in Figure 3. The half of the unsigned magnetic flux underlying the area associated with the brightening observed in AIA 1600 Å are recorded as the temporal profile of the re-connection flux. The kinematics of the filament eruption and the temporal variation in associated reconnection flux are shown in Figure 4.

3. NUMERICAL MODEL

We numerically solve the complete magneto-hydrodynamic equations in three-dimensional spherical coordinates to investigate the early evolution of magnetic flux ropes in the solar corona. For this, we employ the Pencil Code (Pencil Code Collaboration et al. 2021), an open-source, highly modular, and MPI-parallelized code designed for compressible MHD flows [1]. Utilizing a sixth-order finite difference scheme and a third-order Runge-Kutta time-stepping method—among various other options provided by the Pencil Code—we solve the following set of compressible MHD equations.

$$\frac{\mathrm{D} \ln \rho}{\mathrm{D}t} = -\nabla \cdot \mathbf{U} \tag{1}$$

[1] http://pencil-code.nordita.org

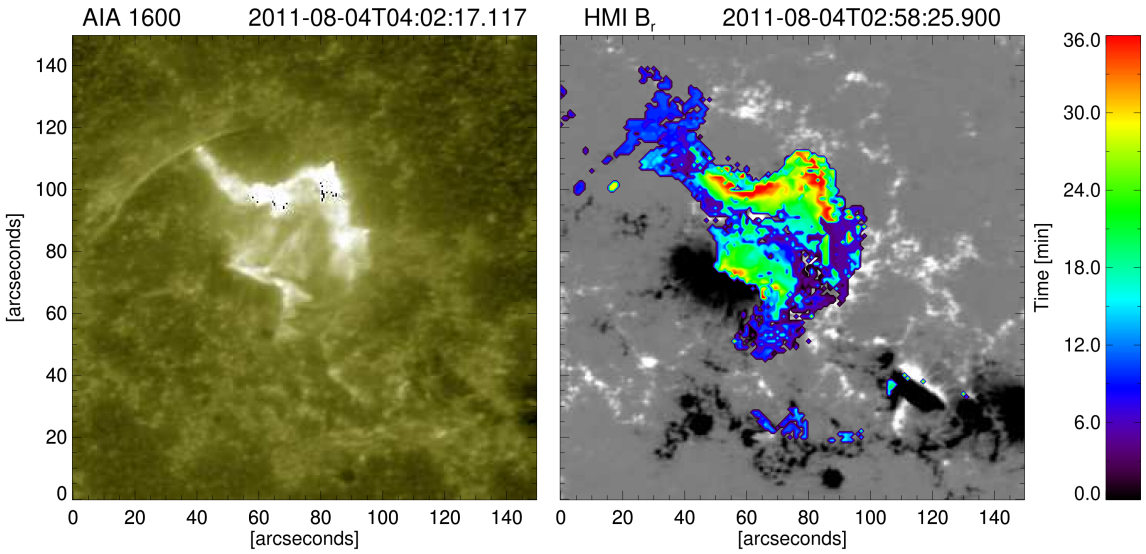

Figure 3. Left panel: Flare associated brightening observed in AIA 1600 Å channel during the flare occurred in AR 11261. Right panel: The associated HMI B_r magnetic field (gray color scale with saturation value ±500 Gauss) and the temporal evolution of the flare ribbons from 03:41 UT to 04:17 UT on 2011 August 04 .

$$\frac{\mathrm{D}\mathbf{U}}{\mathrm{D}t} = -\frac{\nabla p}{\rho} + \frac{GM_\odot}{r^2}\hat{\mathbf{r}} + \frac{\mathbf{J}\times\mathbf{B}}{\rho} + \mathbf{F}_{\rm corr} + \rho^{-1}\mathbf{F}_{\rm visc} \quad (2)$$

$$\frac{\partial \mathbf{A}}{\partial t} = \mathbf{U}\times\mathbf{B} - \eta\mu_0\mathbf{J} \quad (3)$$

$$\rho c_v T\frac{\mathrm{D}\ln T}{\mathrm{D}t} = -\rho c_v T(\gamma-1)\nabla\cdot\mathbf{U} + \eta\mu_0\mathbf{J}^2 + 2\rho\nu \mathsf{S}_{ij}^2 + \nabla\cdot\mathbf{q}_{\rm cond} - \rho^2\Lambda(T) + \mathcal{H} + \rho\zeta_{\rm shock}\left(\nabla\cdot\mathbf{U}\right)^2 \quad (4)$$

In the above, $\mathbf{U}$ is the velocity field; $\mathbf{B}$ is the magnetic field; $\mathbf{A}$ is the magnetic potential; $\mathbf{J}$ is the current density; ρ, p and T are, respectively, the plasma density, pressure and temperature of the system. The viscous force is modelled as

$$\rho^{-1}\mathrm{F}_{\rm visc} = \nabla\cdot(2\rho\nu\mathbf{S}) + \nabla\left(\rho\zeta_{shock}\nabla\cdot\mathbf{U}\right) \quad (5)$$

where ν is kinematic viscosity and S is the traceless rate-of-strain tensor. Additionally, we incorporate a semi-relativistic Boris correction into the classical MHD momentum equation to reduce numerical diffusion and avoid the need for excessively small time steps in MHD simulations, achieved by using an artificially reduced speed of light (Chatterjee 2020).

We include radiative cooling in our model, represented in equation (4), where $\Lambda(T)$ denotes the radiative loss function as described by (Cook et al. 1989). The cooling function is plotted in Figure (5). Furthermore, we use a simplified coronal heating function that varies only with height, following an exponential decay.

$$\mathcal{H} = \frac{F}{L_H}\frac{R_\odot^2}{r^2}\exp\left\{-(r-R_\odot)/L_H\right\} \quad (6)$$

where the input energy flux density is $F = 9.74\times10^5\,\mathrm{erg\,cm^{-2}\,s^{-1}}$ and the decay length is $L_H = 1.948\times10^{10}$ cm.

We have also included field-aligned Spitzer thermal conduction in our model. Here we have used the hyperbolic diffusion equation approach instead of directly including Spitzer conduction in equation (4), similar to Chatterjee (2020).

Let $\mathbf{q}_{\rm cond}$ represents the solution of the non-Fickian transport equation and $\mathbf{q}_{\rm sp}$ denotes the conduction flux according to the Spitzer model. We solve the following equation for the heat flux $\mathbf{q}_{\rm cond}$.

$$\frac{\partial \mathbf{q}_{\rm cond}}{\partial t} = -\frac{\mathbf{q}_{\rm cond}-\mathbf{q}_{\rm sp}}{\tau_{sp}} + \beta(dr\cdot\nabla)^6\mathbf{q}_{\rm cond} \quad (7)$$

where $\mathbf{q}_{\rm sp} = K_{sp}T^{5/2}\hat{\mathbf{b}}(\hat{\mathbf{b}}\cdot\nabla T)$, $\hat{\mathbf{b}}$ denotes the unit vector along the field direction and $K_{sp} = 10^{-6}$ $\mathrm{erg\,K^{-7/2}\,cm^{-1}\,s^{-1}}$. τ_{sp} represents a finite timescale for $\mathbf{q}_{\rm cond}$ to evolve toward the Spitzer heat flux and is set to 0.1 s. Our time step varies between 0.1 - 0.3 ms.

The computational domain consists of a spherical wedge with an extent $R_\odot < r < 6R_\odot$, $5\pi/12 < \theta < 7\pi/12$ and $-\pi/9.6 < \phi < \pi/9.6$. It is resolved by a grid of $512\times288\times160$, which is non uniform in r but uniform in θ and ϕ. The grid spacing in r is $dr = 0.002R_\odot$ at the lower boundary which gradually increases in a log-

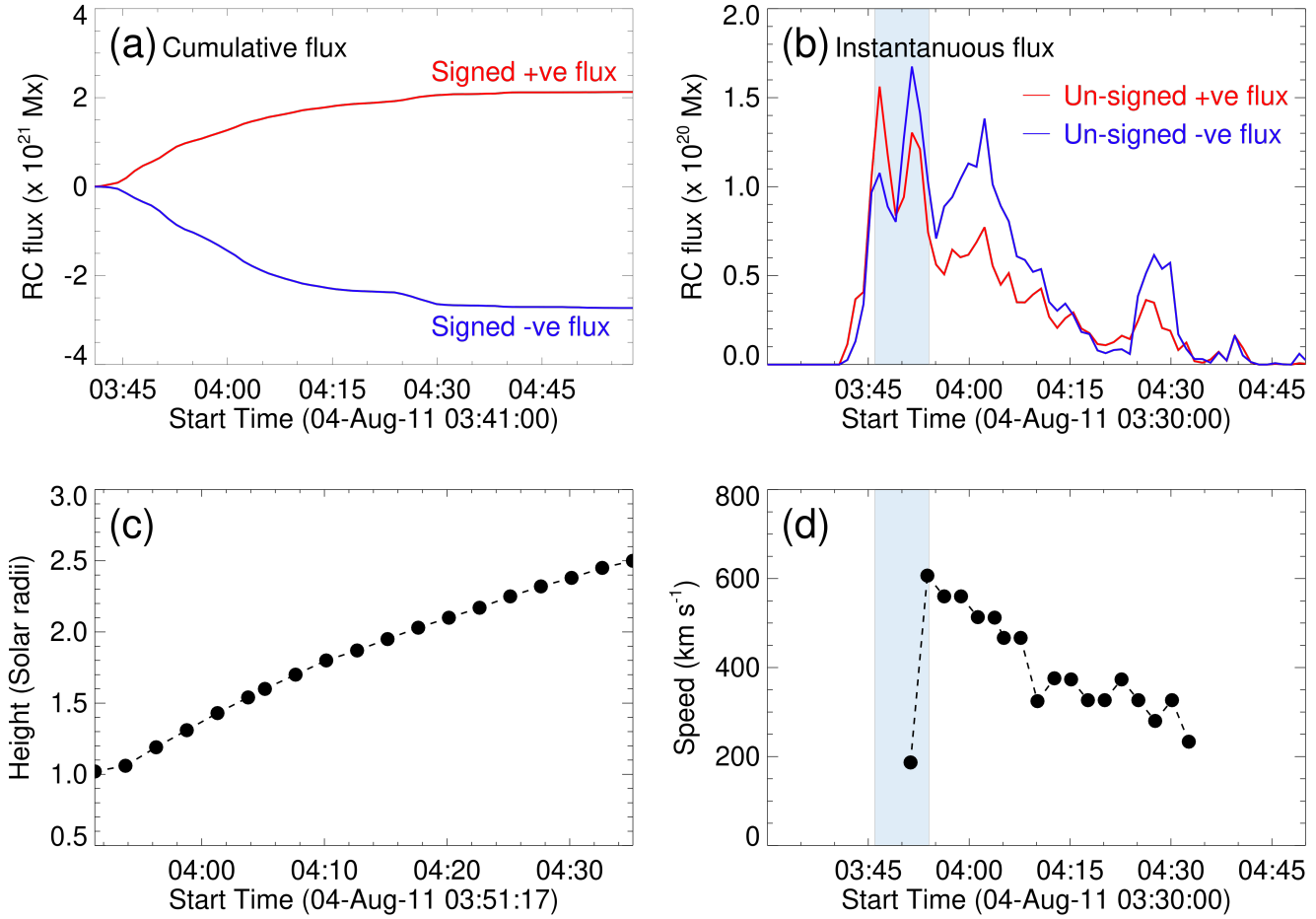

Figure 4. (a) Time profile of signed cumulative reconnection flux integrated over the positive (red) and negative (blue) magnetic polarities underlying the flare ribbons. (b) Time profile of unsigned instantaneous reconnection flux integrated over the positive (red) and negative (blue) magnetic polarities underlying the flare ribbons. (c) Height time plot of the filament leading edge measured from STEREO EUVI, COR1 and COR2 for the same event as shown in Figure 2. (d) Velocity profile of the filament leading edge derived from Panel (c).

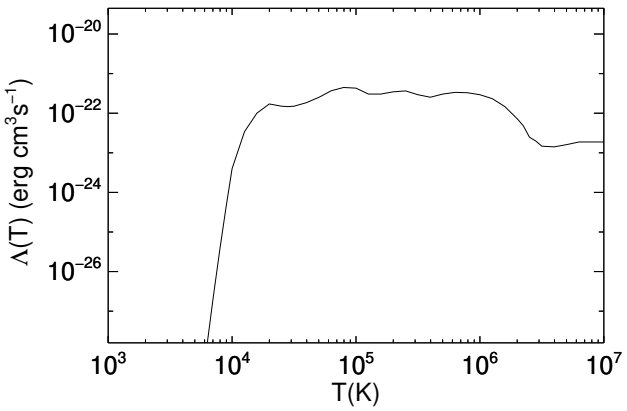

Figure 5. The radiative cooling function in used in this work is a modified version of Cook et al. (1989)

arithmic manner reaching $dr = 0.003R_\odot$ at the upper boundary.

We consider a high-temperature coronal plasma as an ideal gas with an adiabatic constant of $\gamma = 1.66$. Initially, the domain is assumed to be in the state of a hydrostatic equilibrium at a uniform temperature of $T_0 = 10^6$ K with a density stratification given by

$$\rho = \rho_0 \exp\left\{-\frac{R_\odot}{H_p}(1 - \frac{R_\odot}{r})\right\} \tag{8}$$

where, $\rho_0 = 1.0 \times 10^{-15}$ g cm^{-3} is the initial density and $H_{p0} = c_{s0}/g_r$ denotes the initial pressure scale height. The initial atmosphere consists of a pre-existing potential field with arcade like geometry as given in Fan (2012) (see their Equation 12 and 13).

Figure 6. The twisted torus before emerging through the bottom boundary at $r = R_\odot$. The number of turns of one of the field lines is shown in black.

At the lower boundary, we impose an electromotive force given by

$$\mathbf{E}\,|_{r=R_\odot} = -\frac{1}{c}\mathbf{v}_0 \times \mathbf{B}_{\rm torus}(R_\odot, \theta, \phi, t)$$

which bodily transports the twisted torus radially into the domain. The major and minor radius of the torus are $0.25R_\odot$ and $0.042R_\odot$ respectively and with a field line twist rate of $0.068\,{\rm rad\,Mm^{-1}}$. The twist rate indicates the field line winds around the tube axis per unit length along the axis. The flux tube is initially located at $r_0 = 0.705R_\odot$, thus the torus is initially entirely below the surface and moves bodily upward toward the lower boundary at constant speed, until it reaches a height $r_{\rm stop}$ when the emergence is stopped and a part of the torus is still inside of the computational domain. The velocity field at the lower boundary is specified to be uniform in the region where the emerging torus intersects the lower boundary and its zero everywhere else. The imposed emergence speed, $v_0 = 2$ $\rm km\,s^{-1}$, which is much smaller than the Alfven speed v_A $= 1.69$ $\rm Mm\,s^{-1}$ to ensure that the emerging flux rope is allowed to evolve quasi-statically during the flux emergence phase at the lower boundary. When the emergence is stopped, the velocity at the lower boundary is set to zero, with no inflows or outflows and footpoints are rigidly anchored. For the θ boundaries, we assume a non-penetrating stress-free boundary for the velocity field and perfectly electrically conducting walls for the magnetic field. The ϕ boundaries are periodic. For the top boundary, we use a simple outward extrapolating boundary condition that allows plasma and magnetic field to flow through.

In this simulation, we drive the emergence of the torus until $r_{\rm stop} = 0.85R_\odot$ to study the reconnection flux during the evolution of the twisted flux rope in the corona which produces homologous CMEs.

4. RESULTS

Our simulation produces two homologous CME eruptions; each of the eruption characterized by an impulsive increase of the kinetic energy and corresponding release of the magnetic energy. We first briefly discussed the initiation and evolution of the eruptions and then analyze the velocity and reconnection flux of different CME eruptions in the simulation. Note that the magnetic reconnection in our model using MHD approximation is of numerical origin, we cannot resolve length scales smaller than the Larmor radius of the proton or the mean free path. However, our goal here is to find a relation (if any exists) between the reconnection flux and the speed of the ejecta in our simulations.

4.1. *Overview of eruptions*

The simulation begins with a magnetic flux rope (MFR) emerging from the lower boundary and pushing into a pre-existing coronal potential arcade field. The normal magnetic flux distributions at the lower boundary are represented by bipolar bands $B_r(R_\odot, \theta, \phi) = B_s(\theta)$ where the $B_s(\theta)$ denotes the potential arcade field at the lower boundary, as shown in Figure (7). The emergence process is halted once a specified amount of twisted flux is driven into the corona. Although the imposed emergence of a twisted flux rope through the lower boundary may not perfectly reflect real-world conditions, it serves as a means to achieve a sequence of near-force-free coronal flux rope equilibria with increasing amounts of locally detached, twisted flux. In all cases, we observe the development of current layers with a sigmoid morphology beneath the flux rope. Magnetic reconnection within these current layers continues to add flux to the flux rope, even though the total magnetic energy gradually decreases due to reconnections. This continuous addition of flux facilitates successive eruptions.

The first eruption is triggered when the twist of the winding of the flux rope field lines about the torus axis reaches approximately 1 wind between the anchored foot points. We stopped the emergence of the twisted torus tube at 33.5 hours when the extent of the flux rope that emerged is such that the field line's winding about the flux rope's axis is 1.5 between anchored footpoints. This is estimated in a simple way by multiplying the total number of winds around the circular torus, i.e., 5 winds, by the fraction of the torus circumference above the solar surface. The second eruption began after we stopped the flux emergence. The helical kink instability is expected to develop in a line-tied coronal flux rope if the

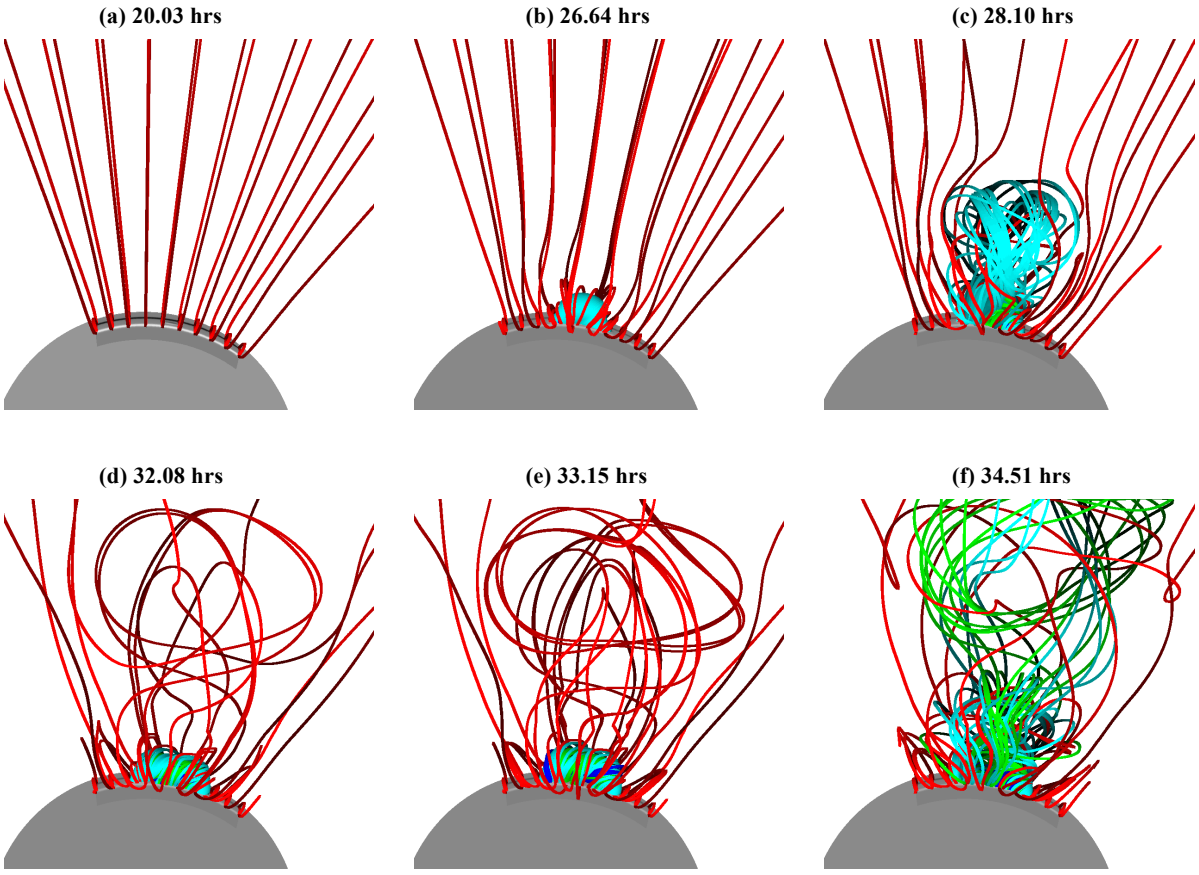

Figure 7. The 3D evolution of the magnetic field of the twisted flux rope emerging into the corona at the specified times (in hours). Red field lines have footpoints in the ambient arcade, while blue, green, and cyan field lines originate from the emerging flux region. An animation of this evolution is available in the online paper.

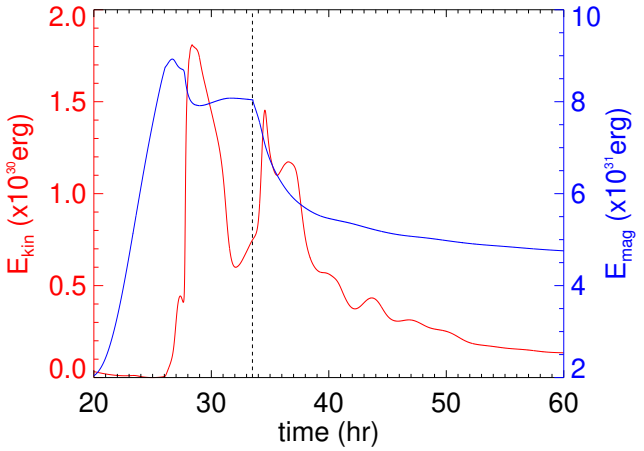

Figure 8. Total kinetic energy E_{kin} (red) and total magnetic energy E_{mag} (blue) as a function of time. The dashed vertical line represents the time when the flux emergence stops.

total windings of the field line twist around the axis exceed a critical value between the line-tied ends (Hood & Priest 1981; Török & Kliem 2003; Török et al. 2004). This critical value is 1.25, based on the analytical calculation of a uniformly twisted cylindrical flux tube (Hood & Priest 1981). The animation (corresponding to Figure 7) clearly shows substantial writhing motion at the onset of the eruption for the second eruption but not in first eruption, indicative of the helical kink instability. Figure 8 illustrates the evolution of kinetic and magnetic energies for both eruptions. The time at which the kinetic energy reaches its peak is designated as the eruption time.

Furthermore, we examined whether the flux rope is also unstable to the torus instability (Bateman 1978; Kliem & Török 2006; Isenberg & Forbes 2007), which is triggered by a vertical force imbalance between the upward hoop force and the downward strapping force acting on the magnetic flux rope (MFR). The external strapping field is assumed to be the potential field B_p

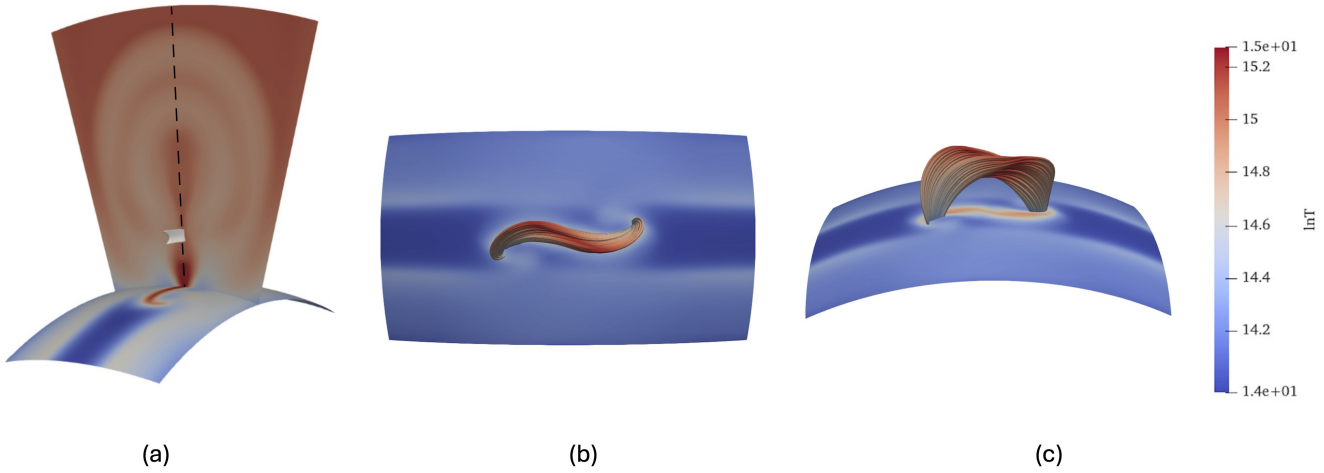

Figure 9. Identification of current sheet and field lines of the flux rope from different viewing angles. The current sheet (in white) traced from the temperature isosurface with a value $\log_{10} T = 6.6$ shown in panel (a). The field lines passing through such sheets gives the reconnection flux. The sigmoid fieldlines are shown in panels (b) and (c). The time in all these panels are taken at $t = 27.32$ hours.

with the same normal distribution at the lower boundary. The rate of decline with height is measured by the decay index $n = -d \ln B_h / d \ln h$. The critical decay index for a 3D line-tied arched flux rope has been calculated by Isenberg & Forbes (2007) to be close to 1.7. In this work, for a decay index of 1.7, the critical heights are 1.21 $R_\odot$ and 1.28 $R_\odot$, respectively for the two successive eruptions. The height of the apex of the axial field line of the coronal flux rope, estimating it to be 1.6 $R_\odot$ and 1.7 $R_\odot$ for the two successive CMEs at the time of eruption calculated by tracking the flux rope over the course of their evolution (see Appendix). For both eruptions, the flux rope crosses the critical threshold of height, indicating that it is also torus unstable. This indicates the fundamental role of kink instability and torus instability in triggering ejective eruptions of a 3D line-tied coronal flux rope.

4.2. *Evolution of velocity and reconnection flux*

The panels (a) and (b) of Figure 10 illustrate the radial velocity of the flux rope during both eruptions. These velocities were determined by tracking the apex of each flux rope throughout their evolution (see Appendix). The first ejection has a peak radial velocity of $224\,\mathrm{km\,s^{-1}}$, which is slightly higher than the $213\,\mathrm{km\,s^{-1}}$ velocity of the second CME. This observation is understood by the time versus kinetic energy plot, which shows the second CME registered lower kinetic energy than its precursor. The initial eruption occurs at a radial distance of $1.9R_\odot$, while the second eruption takes place at $1.8R_\odot$. Due to the lower velocity of the second eruption, there is no interaction between the two CMEs. An interesting observation is that the velocity starts to decrease after the eruption which is also observed in observational data. This could be attributed to the absence of solar wind, which normally drives the magnetic flux rope (MFR) further into the heliosphere post-eruption.

The panels (c) and (d) of Figure 10 depicts the changes in reconnection flux over time for both eruptions. We monitored the hottest region beneath the flux rope in the r-θ plane both before and after the eruption as shown in Figure 9). This region corresponds to the current sheet, as the current sheet typically exhibits higher temperatures compared to the surrounding areas. By tracking the same hottest region, we can effectively identify the current sheet and quantify the flux passing through it. The total reconnection flux passing through the is given by

$$\phi_{RC} = \int B_n \, dS = \int B_r \, dA$$

where B_n represents the magnetic flux normal to the elemental area dS of the current sheet, and B_r is the radial magnetic field in the ribbons, which are the footpoints of newly reconnected magnetic field lines at the lower boundary. The term dA denotes the elemental area of these footpoints. Thus reconnection flux is determined by calculating the magnetic flux swept by the field lines passing the lower boundary. Direct measurement

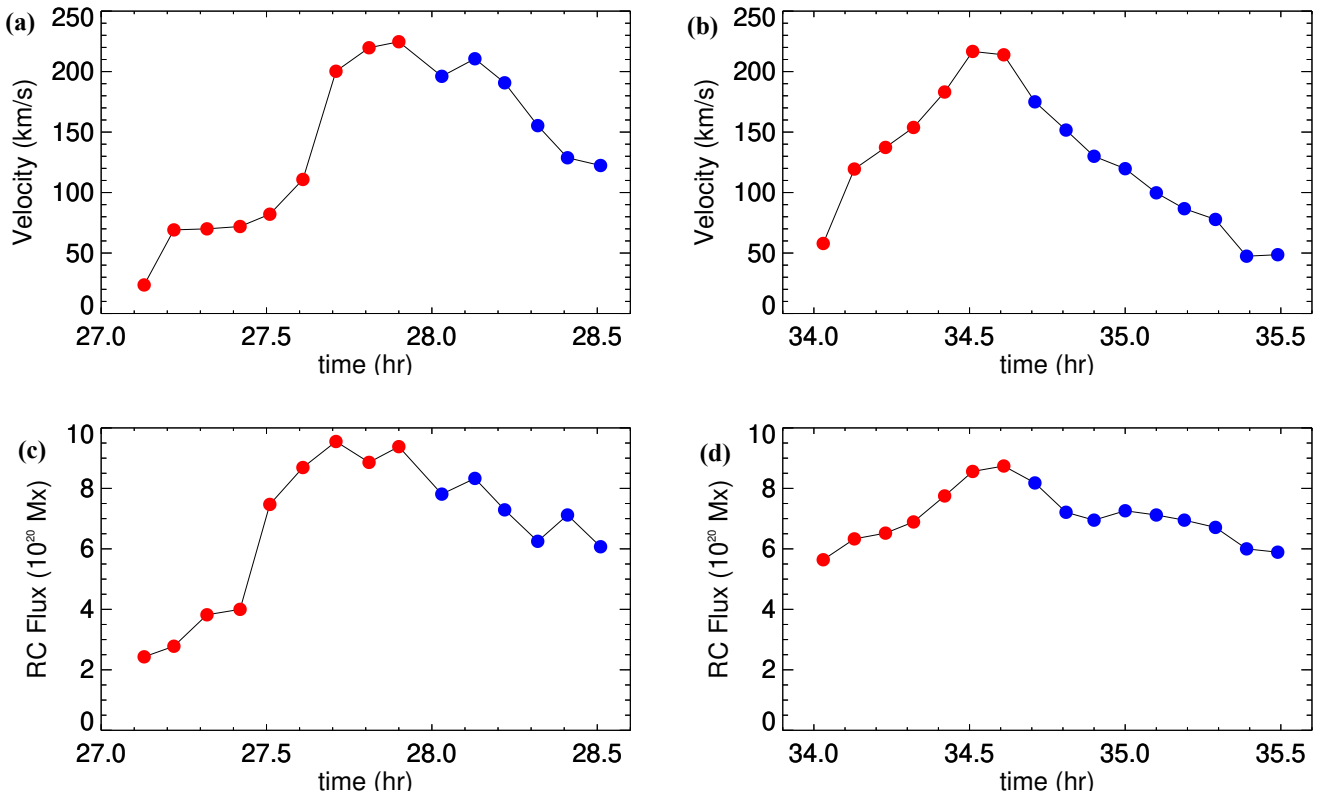

Figure 10. Time evolution of velocity, (a)-(b), and reconnection flux, (c)-(d), for both the eruptions in the simulation. The velocity is calculated by tracking the flux rope in the central meridional plane. The reconnection flux is calculated by the magnetic flux passing through the footpoints of the fieldlines as well as through the current sheet shown in Fig. 9a. The red (blue) circles are used to represent simulation data before (after) the eruption.

of B_n and dS within the current sheet is not feasible, even in simulations, due to the intricate structure of the reconnection sheet. However, B_r and dA are relatively straightforward to calculate, even for a spherical wedge-shaped domain. Therefore, this approach provides an indirect but well-defined measure of the magnetic flux passing through the reconnection sheet. This method allows for an effective evaluation of the magnetic reconnection process by focusing on the measurable quantities at the footpoints, offering valuable insights into the dynamics of the reconnection events.

The peak reconnection flux (RC flux) for the first and second eruptions are 9×10^{20} Mx and 8.5×10^{20} Mx, respectively. The panels (c) and (d) of Figure 10 indicate that the reconnection flux decreases after reaching its peak value, with the eruptions occurring near the maximum reconnection flux. This phenomenon might be explained by the intricacies of calculating the RC flux. When an eruption occurs, the RC sheet breaks down, making it challenging to track the field lines passing through the current sheet (CS). Despite this complexity, similar patterns are observed in observational data (see panel (b) of Figure 4, suggesting a consistent underlying process. The observed decrease in reconnection flux post-peak might be tied to the dynamic changes within the RC sheet during an eruption. As the RC sheet disintegrates, accurately measuring and tracking the magnetic field lines through the CS becomes challenging. This complexity impacts the calculated values of RC flux, reflecting the real-time physical changes occurring during an eruption. Moreover, these findings align with observational data, further validating the temporal relation between the reconnection flux and the onset of eruptions (panels b-d of Fig. 4). This highlights the importance of considering both the peak and the subsequent decrease in reconnection flux when studying the dynamics of solar eruptions and magnetic reconnection events.

4.3. *Correlation between MFR velocity and reconnection flux*

The panels (a) and (b) of Figure 11 show scatter plots of the magnetic flux rope (MFR) radial velocity (v_r) versus the reconnection flux (ϕ_{RC}). Both before and after the eruption, the radial velocity exhibits a lin-

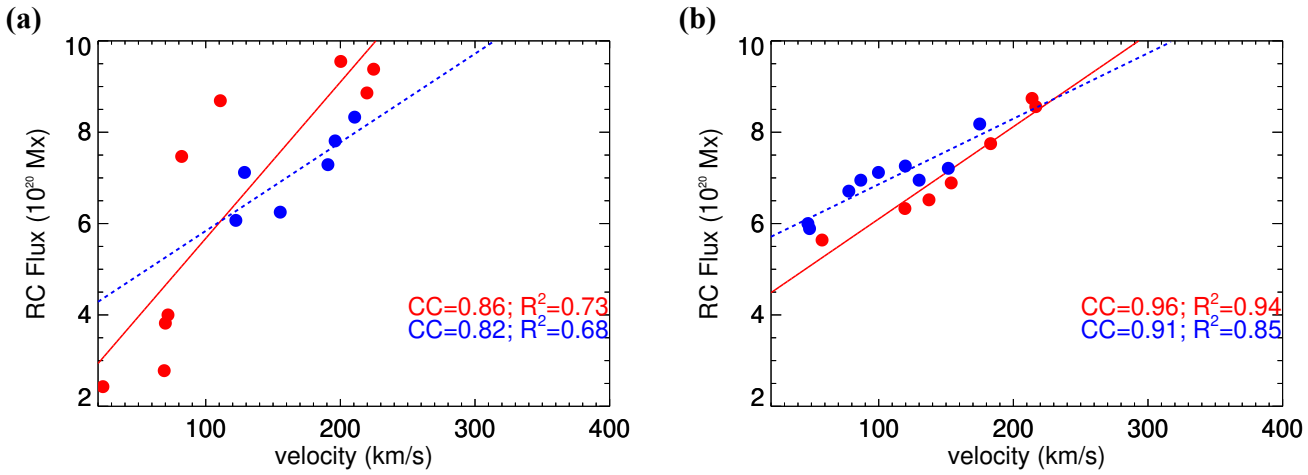

Figure 11. (a) CME reconnection flux vs velocity plot for the first eruption. The red (blue) circles are used to represent before (after) the eruption, respectively. The solid (dashed) line is the linear fit to the points before (after) the eruption, respectively. (b) Same as (a) but for the second eruption.

ear relationship with the reconnection flux for the eruptive events. Notably, the Pearson's correlation coefficients before the eruption for the two events are 0.86 and 0.96, respectively, indicating a strong correlation between the reconnection flux and the radial velocity. This strong linear relationship persists post-eruption, with the Pearson's correlation coefficients slightly decreasing to 0.82 and 0.91, respectively. This indicates the significant influence of reconnection flux on the radial velocity of CMEs. A similar qualitative relationship is also observed in the case of observational data (see panel (d) of Figure 4) where the velocity of the erupting filament and the associated reconnection flux simultaneously increase as indicated by the cyan shaded region. Due to observational constraints (limited time-cadence of STEREO EUVI), it was challenging to gather more data points during the initial acceleration phase of the eruption. After the peak acceleration phase, both the velocity and reconnection flux exhibit a monotonically decreasing temporal profile while maintaining similar correlated behavior. The numerical analysis from our simulation complements the above-mentioned observational results, allowing us to determine the temporal evolution of the reconnection flux and velocity and their correlation.

5. SUMMARY AND DISCUSSION

Through a simple and efficient MHD simulation, we demonstrated that homologous CMEs can result from the repeated formation and partial eruption of unstable flux ropes during the sustained emergence of highly twisted magnetic fields in an active region. Our results show that, with the continuous emergence of flux, a new current sheet (CS) forms above the same polarity inversion line (PIL) after the completion of a previous eruption, leading to a new eruption. This recurring formation and disruption of coronal CS, driven by the ongoing emergence of flux within a single bipolar configuration, results in homologous eruptions.

Our simulation began with the emergence of a twisted flux rope at the lower boundary into a pre-existing coronal arcade. We found that the flux rope initially settles into a quasi-static rise phase, with an underlying sigmoid-shaped current layer developing beneath the flux rope. This current layer is likely the site for the formation of thin current sheets and magnetic reconnection (Titov 2007; Aulanier et al. 2005; Savcheva et al. 2012). The reconnection in the current layer effectively adds twisted flux to the magnetic flux rope, allowing it to rise quasi-statically before undergoing a partial eruption. Subsequent flux emergence forms a new current channel, which exhibits similar behavior and erupts after the emergence stops.

In both eruptions, the magnetic flux rope (MFR) demonstrates torus instability after reaching a height $\sim 1.6R_{\odot}$. The first eruption remains stable to helical kink instability, while the second eruption is kink unstable. The subsequent CME, in our simulation, has a slighly lower speed and lower kinetic energy. Initially, the reconnection flux increases, followed by a gradual decrease, after each eruption. These trends are consistent with the observation of an eruptive event. Our simulation indicates that the reconnection process significantly influences the evolution of the MFR. The reconnection flux shows a linear correlation with the velocity, both before and after the eruption. This result indicates that reconnection may play an important role in propelling the magnetic ejecta after the loss of equilibrium phase.

Although our numerical simulation model does not include the solar wind, the inclusion of radiative cooling and explicit coronal heating makes it more realistic than previously published homologous solar eruption models (Chatterjee & Fan 2013; Bian et al. 2022). We account for localized heating due to the formation and dissipation of current sheets in the corona, as well as the redistribution of heat through field-aligned conduction. The lower boundary of our simulation domain is positioned at the coronal base rather than the chromosphere, and therefore, our model does not simulate prominence formation. Our simulations also demonstrate that, with a more realistic adiabatic index of $\gamma = 5/3$, which results in stronger adiabatic cooling of the expanding flux rope, and with an explicit treatment of heating and heat transport, the erupting flux rope is still able to achieve speeds typical for the lower corona.

Although we employ an analytical configuration of the magnetic flux rope (MFR) and include various physical processes in our model, this approach may not fully represent the realistic conditions of the solar eruptions. To address the complexity and evolution of the magnetic configuration in a real scenario, a detailed and accurate description of the evolving magnetic field is essential. Our future goal is to conducting detailed analysis of solar eruptions that are directly driven or constrained by photospheric magnetograms is crucial for obtaining an accurate understanding.

The work was supported by Indo-US Science and Technology Forum (IUSSTF/JC-113/2019). SSM acknowledge NOVA HPC and VINO server of IIA used to perform the numerical simulation and analysis. P.C. acknowledges the DiRAC Data Intensive service (DIaL2) at the University of Leicester (project id: dp261), managed by the University of Leicester Research Computing Service on behalf of the STFC DiRAC HPC Facility (www.dirac.ac.uk). The DiRAC service at Leicester was funded by BEIS, UKRI and STFC capital funding and STFC operations grants. DiRAC is part of the UKRI Digital Research Infrastructure. P.C. also acknowledges the allocation of computing resources at the PDC Center for High Performance Computing at KTH in Stockholm, funded by the National Academic Infrastructure for Supercomputing in Sweden. RS acknowledges support from the project EFESIS (Exploring the Formation, Evolution and Space-weather Impact of Sheath-regions), under the Academy of Finland Grant 350015. Additionally, authors thank the NASA SDO team for providing valuable HMI and AIA data. SDO is a mission under NASA's Living with a Star program. Open access is funded by Helsinki University Library.

REFERENCES

Amari, T., Luciani, J. F., Aly, J. J., Mikic, Z., & Linker, J. 2003, ApJ, 585, 1073, doi: 10.1086/345501

Antiochos, S. K., DeVore, C. R., & Klimchuk, J. A. 1999, ApJ, 510, 485, doi: 10.1086/306563

Archontis, V., & Hood, A. W. 2008, ApJL, 674, L113, doi: 10.1086/529377

Archontis, V., Hood, A. W., Savcheva, A., Golub, L., & Deluca, E. 2009, ApJ, 691, 1276, doi: 10.1088/0004-637X/691/2/1276

Aulanier, G. 2014, in Nature of Prominences and their Role in Space Weather, ed. B. Schmieder, J.-M. Malherbe, & S. T. Wu, Vol. 300, 184–196, doi: 10.1017/S1743921313010958

Aulanier, G., Pariat, E., & Démoulin, P. 2005, A&A, 444, 961, doi: 10.1051/0004-6361:20053600

Aulanier, G., Török, T., Démoulin, P., & DeLuca, E. E. 2010, ApJ, 708, 314, doi: 10.1088/0004-637X/708/1/314

Bateman, G. 1978, MHD instabilities (The MIT Press)

Bein, B. M., Berkebile-Stoiser, S., Veronig, A. M., Temmer, M., & Vršnak, B. 2012, ApJ, 755, 44, doi: 10.1088/0004-637X/755/1/44

Bian, X., Jiang, C., Feng, X., Zuo, P., & Wang, Y. 2022, ApJL, 925, L7, doi: 10.3847/2041-8213/ac4980

Chatterjee, P. 2020, Geophysical and Astrophysical Fluid Dynamics, 114, 213, doi: 10.1080/03091929.2019.1672676

Chatterjee, P., & Fan, Y. 2013, ApJL, 778, L8, doi: 10.1088/2041-8205/778/1/L8

Chatterjee, P., Hansteen, V., & Carlsson, M. 2016, PhRvL, 116, 101101, doi: 10.1103/PhysRevLett.116.101101

Chen, J. 2017, Physics of Plasmas, 24

Chen, J. 2017, Physics of Plasmas, 24, 090501, doi: 10.1063/1.4993929

Chen, P. F. 2011, Living Reviews in Solar Physics, 8, 1, doi: 10.12942/lrsp-2011-1

Chen, P. F., & Shibata, K. 2000, ApJ, 545, 524, doi: 10.1086/317803

Cheng, X., Zhang, J., Liu, Y., & Ding, M. D. 2011, ApJL, 732, L25, doi: 10.1088/2041-8205/732/2/L25

Cook, J. W., Cheng, C. C., Jacobs, V. L., & Antiochos, S. K. 1989, ApJ, 338, 1176, doi: 10.1086/167268

DeVore, C. R., & Antiochos, S. K. 2008, ApJ, 680, 740, doi: 10.1086/588011

Duan, A., Jiang, C., He, W., et al. 2019, ApJ, 884, 73, doi: 10.3847/1538-4357/ab3e33
Dun, J., Kurokawa, H., Ishii, T. T., Liu, Y., & Zhang, H. 2007, ApJ, 657, 577, doi: 10.1086/510373
Fan, Y. 2001, ApJL, 554, L111, doi: 10.1086/320935
—. 2010, ApJ, 719, 728, doi: 10.1088/0004-637X/719/1/728
—. 2012, ApJ, 758, 60, doi: 10.1088/0004-637X/758/1/60
Forbes, T. G., & Priest, E. R. 1984, SoPh, 94, 315, doi: 10.1007/BF00151321
Forbes, T. G., Linker, J. A., Chen, J., et al. 2006, SSRv, 123, 251, doi: 10.1007/s11214-006-9019-8
Gibson, S. E., & Fan, Y. 2006, Journal of Geophysical Research (Space Physics), 111, A12103, doi: 10.1029/2006JA011871
Gopalswamy, N., Yashiro, S., Akiyama, S., & Xie, H. 2017, SoPh, 292, 65, doi: 10.1007/s11207-017-1080-9
Hood, A. W., & Priest, E. R. 1981, Geophysical and Astrophysical Fluid Dynamics, 17, 297, doi: 10.1080/03091928108243687
Howard, R. A., Moses, J. D., Vourlidas, A., et al. 2008, SSRv, 136, 67, doi: 10.1007/s11214-008-9341-4
Hu, Q. 2017, Science China Earth Sciences, 60, 1466
Isenberg, P. A., & Forbes, T. G. 2007, ApJ, 670, 1453, doi: 10.1086/522025
Janvier, M., Aulanier, G., & Démoulin, P. 2015, SoPh, 290, 3425, doi: 10.1007/s11207-015-0710-3
Kazachenko, M. D. 2023, arXiv e-prints, arXiv:2310.02878, doi: 10.48550/arXiv.2310.02878
Kazachenko, M. D., Lynch, B. J., Welsch, B. T., & Sun, X. 2017, ApJ, 845, 49, doi: 10.3847/1538-4357/aa7ed6
Kliem, B., & Török, T. 2006, PhRvL, 96, 255002, doi: 10.1103/PhysRevLett.96.255002
Kopp, R. A., & Poletto, G. 1986, in The Sun and the Heliosphere in Three Dimensions, ed. R. G. Marsden & L. A. Fisk, Vol. 123, 65, doi: 10.1007/978-94-009-4612-5_8
Lemen, J. R., Title, A. M., Akin, D. J., et al. 2012, SoPh, 275, 17, doi: 10.1007/s11207-011-9776-8
Li, Y., Lynch, B. J., Welsch, B. T., et al. 2010, SoPh, 264, 149, doi: 10.1007/s11207-010-9547-y
Liu, R. 2020, Research in Astronomy and Astrophysics, 20, 165
Lynch, B. J., Antiochos, S. K., DeVore, C. R., Luhmann, J. G., & Zurbuchen, T. H. 2008, ApJ, 683, 1192, doi: 10.1086/589738
Magara, T. 2004, ApJ, 605, 480, doi: 10.1086/382148
Martínez-Sykora, J., Hansteen, V., & Carlsson, M. 2008, ApJ, 679, 871, doi: 10.1086/587028
Nitta, N. V., & Hudson, H. S. 2001, Geophys. Res. Lett., 28, 3801, doi: 10.1029/2001GL013261
Patsourakos, S., Vourlidas, A., & Stenborg, G. 2013, ApJ, 764, 125, doi: 10.1088/0004-637X/764/2/125
Patsourakos, S., Vourlidas, A., Török, T., et al. 2020, SSRv, 216, 131, doi: 10.1007/s11214-020-00757-9
Pencil Code Collaboration, Brandenburg, A., Johansen, A., et al. 2021, The Journal of Open Source Software, 6, 2807, doi: 10.21105/joss.02807
Qiu, J., Wang, H., Cheng, C. Z., & Gary, D. E. 2004, ApJ, 604, 900, doi: 10.1086/382122
Ranns, N. D. R., Harra, L. K., Matthews, S. A., & Culhane, J. L. 2000, A&A, 360, 1163
Régnier, S., & Canfield, R. C. 2006, A&A, 451, 319, doi: 10.1051/0004-6361:20054171
Romano, P., Elmhamdi, A., Falco, M., et al. 2018, ApJL, 852, L10, doi: 10.3847/2041-8213/aaa1df
Romano, P., Zuccarello, F., Guglielmino, S. L., et al. 2015, A&A, 582, A55, doi: 10.1051/0004-6361/201525887
Sarkar, R., Srivastava, N., & Veronig, A. M. 2019, The Astrophysical Journal Letters, 885, L17, doi: 10.3847/2041-8213/ab4da2
Savcheva, A., Pariat, E., van Ballegooijen, A., Aulanier, G., & DeLuca, E. 2012, ApJ, 750, 15, doi: 10.1088/0004-637X/750/1/15
Schmieder, B., Démoulin, P., & Aulanier, G. 2013, Advances in Space Research, 51, 1967
Schou, J., Scherrer, P. H., Bush, R. I., et al. 2012, SoPh, 275, 229, doi: 10.1007/s11207-011-9842-2
Shibata, K., & Magara, T. 2011, Living Reviews in Solar Physics, 8, 6, doi: 10.12942/lrsp-2011-6
Sterling, A. C., & Moore, R. L. 2001, J. Geophys. Res., 106, 25227, doi: 10.1029/2000JA004001
Temmer, M., Veronig, A. M., Vršnak, B., et al. 2008, ApJL, 673, L95, doi: 10.1086/527414
Thompson, W. T., Davila, J. M., Fisher, R. R., et al. 2003, in Society of Photo-Optical Instrumentation Engineers (SPIE) Conference Series, Vol. 4853, Innovative Telescopes and Instrumentation for Solar Astrophysics, ed. S. L. Keil & S. V. Avakyan, 1–11, doi: 10.1117/12.460267
Titov, V. S. 2007, ApJ, 660, 863, doi: 10.1086/512671
Titov, V. S., & Démoulin, P. 1999, A&A, 351, 707
Török, T., & Kliem, B. 2003, A&A, 406, 1043, doi: 10.1051/0004-6361:20030692
Török, T., Kliem, B., & Titov, V. S. 2004, A&A, 413, L27, doi: 10.1051/0004-6361:20031691
van Ballegooijen, A. A., & Martens, P. C. H. 1989, ApJ, 343, 971, doi: 10.1086/167766
Wang, Y., Zhuang, B., Hu, Q., et al. 2016, Journal of Geophysical Research (Space Physics), 121, 9316, doi: 10.1002/2016JA023075

Wuelser, J.-P., Lemen, J. R., Tarbell, T. D., et al. 2004, in Society of Photo-Optical Instrumentation Engineers (SPIE) Conference Series, Vol. 5171, Telescopes and Instrumentation for Solar Astrophysics, ed. S. Fineschi & M. A. Gummin, 111–122, doi: 10.1117/12.506877

Wyper, P. F., Antiochos, S. K., & DeVore, C. R. 2017, Nature, 544, 452, doi: 10.1038/nature22050

Xu, Z., Yang, K., Guo, Y., et al. 2017, ApJ, 851, 30, doi: 10.3847/1538-4357/aa9995

Zhang, J., Dere, K. P., Howard, R. A., Kundu, M. R., & White, S. M. 2001, ApJ, 559, 452, doi: 10.1086/322405

Zhang, J., & Wang, J. 2002, ApJL, 566, L117, doi: 10.1086/339660

Zhang, Y., Liu, J., & Zhang, H. 2008, SoPh, 247, 39, doi: 10.1007/s11207-007-9089-0

6. APPENDIX

The height-time plot is produced by tracking the dark region in the $r - \theta$ plane of the temperature profile, which represents the MFR. By following this dark region consistently, we determine the MFR's velocity during the flux rope's evolution.

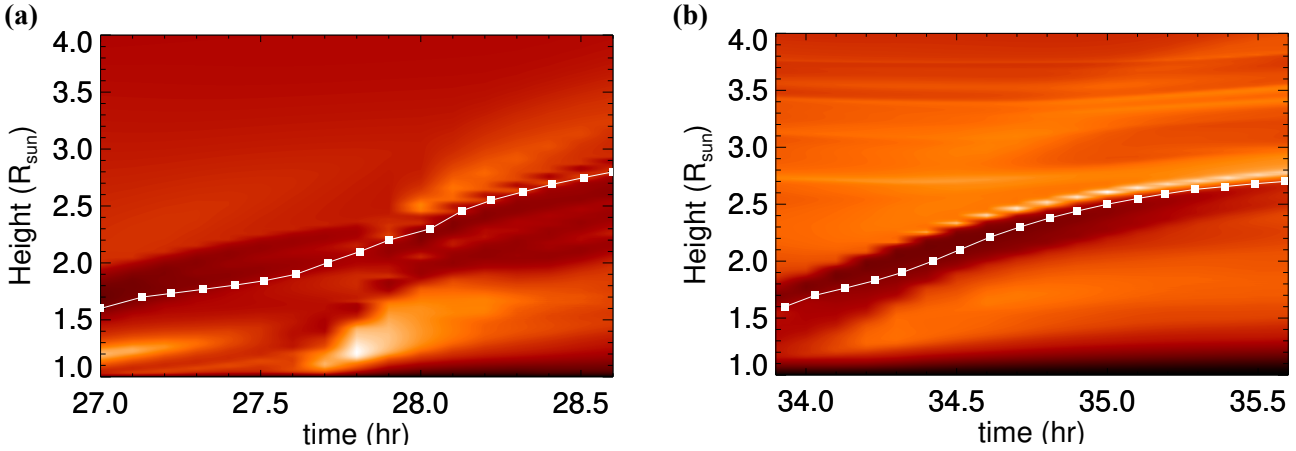

Figure 12. (a) Height time profile of the flux rope before and after the first eruption at $t = 27.9$ hours. The height is calculated by tracking the dark region (flux rope) in the temperature profile. (b) Same as (a), but for the second eruption at $t = 34.7$ hours.

The variation in reconnection flux over time is attributed to changes in the area of the foot points of the field lines near the lower boundary at a height of $1.04R_{\odot}$. This relationship is illustrated for both eruptions, with the corresponding areas plotted over time in Figures 13. These plots provide a detailed representation of how the swept area evolves and influences the reconnection flux during each eruption.

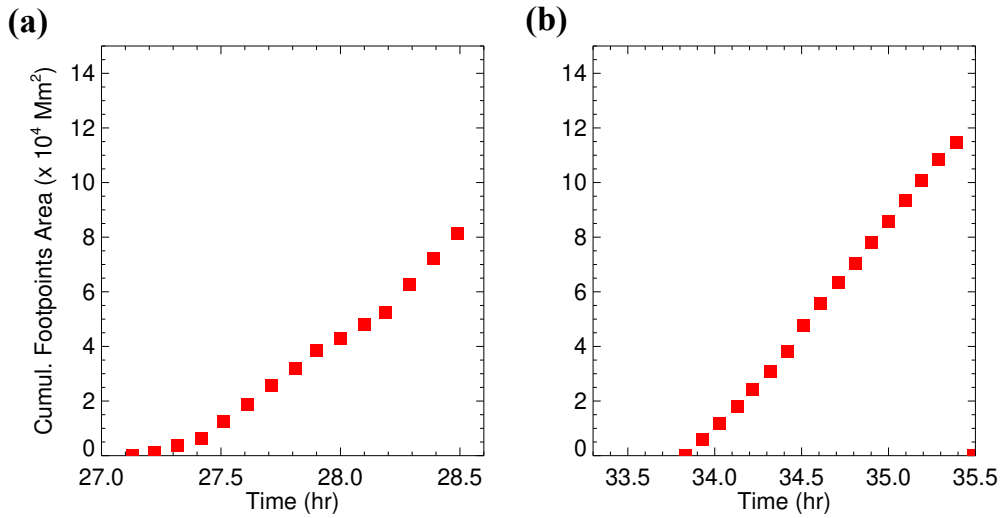

Figure 13. Cumulative area of footpoints of the fieldlines passing through the the reconnection sheet for the first (a) and second eruption (b), respectively.